Short-Range−Long-Range Order Transformation in the $Bi_4V_{2-x}Fe_xO_{11-y}$ Series

E. García-González, M. Arribas, and J. M. González-Calbet*

Facultad de Químicas, Departamento de Química Inorgánica, Universidad Complutense, 28040-Madrid, Spain

Received May 12, 2000. Revised Manuscript Received August 3, 2000

In the present work, we have studied the $Bi_4V_{2-x}Fe_xO_{11-y}$ series in the full range of composition. The microstructural characterization performed by means of X-ray powder diffraction, electron diffraction, and high-resolution electron microscopy reveals the crystals as formed by two kind of domains, structurally related, which differ in the V(Fe)−O layers. Both types of domains intergrow in variable ratio as a function of the iron content, but they appear to contain vanadium and iron in a random distribution. The doping process is not a simple substitution process, and microstructure in both areas together with chemical composition is interpreted in terms of short-range−long-range ordering of the V−O and Fe−O polyhedra in the perovskite layers of the basic structure.

Introduction

The first evidence of high oxide ion conductivity in an alternate $(Bi_2O_2)^{2+}$ layer/perovskite layer structure was published in 1988 by Abraham et al.[1] The new compound discovered by these authors, $Bi_4V_2O_{11}$, can be formulated as $(Bi_2O_2)^{2+}(VO_{3.5})^{2-}$, the perovskite layer being oxygen deficient. $Bi_4V_2O_{11}$ exhibits two reversible phase transitions: $\alpha \leftrightarrows \beta$ at 450 °C and $\beta \leftrightarrows \gamma$ at 570 °C.[1−5] The random oxide ion vacancies distribution above 570 °C seems to be responsible for the remarkably high ionic conductivity in the γ-domain: 0.1−1 $S \cdot cm^{-1}$.

Because of the attractive conduction properties of the γ-form, attempts to stabilize this phase at room temperature were undertaken using a doping strategy. The substitution of vanadium by other metallic ions was successfully done with different elements and led to a new family of materials designated by the acronym BIMEVOX.[6] The ensemble of the experimental results in these phases is not the size or the valence state of the dopant but rather the structural parameter and the ability of the dopant cations to affect the long-range ordering of the mother compound $Bi_4V_2O_{11}$.[7] The lability of the oxygen atoms within the $(VO_{3.5})^{2-}$ layers probably generates long-range modification of the remaining V−O polyhedra when one dopant, with its own preferred coordination, is introduced.

Besides, most of the doping process investigated led to compounds with anionic stoichiometry below O_{11}. $Bi_4V_2O_{11}$ itself can be reduced in a relatively easy way,[8,9] and the presence of V(IV) ions can be interpreted as an in situ doping process. Galy et al.[8] have described the $(Bi_2O_2)_2(V^V_{1-x}V^{IV}_x)_2O_{11-x}$ solid solution, for x values $0 \le x \le 1$, but according to Joubert et al.,[9] the transformation V(V) ⇒ V(IV) is limited to one-third of the V(V) ions, thus leading to the $Bi_4V_2O_{10.66}$ ($Bi_6V_3O_{16}$) composition. The V−O layers are constituted by isolated V_3O_{10} units, in which a $V^{IV}O_6$ octahedron shares vertex with two V^VO_4 tetrahedra.[9] The alternate orientation of VO_4 tetrahedra from one unit to the next tripled the b axis of the basic structure, and the absence of connection between them causes the insulating behavior of this compound.

When only V(IV) is present, the $Bi_4V_2O_{10}$ phase is formed and the perovskite-type layers appear to be constituted by square pyramids.[8,10]

As a general fact, the main features of the structure of these materials are well-known, but microscopic details concerning location as well as coordination environment of vanadium are not. In this sense, the problems of defining the crystallography of the V−O layers are probably due to the fact that it contains several V−O polyhedra interconnected according to some order responsible for the 6-fold modulation observed along the b^* direction in α-$Bi_4V_2O_{11}$. For the doped compounds, the problem remains the same. Most investigations of the BIMEVOX phases have been concentrated on the electrical properties,[11] but a complete understanding of the oxygen diffusion process and

* To whom correspondence should be addressed. E-mail: jgcalbet@eucmax.sim.ucm.es.

(1) Abraham, F.; Debreuille-Gresse, M. F.; Mairesse, G.; Nowogrocki, G. *Solid State Ionics* **1988**, *28*, 529.
(2) Varma, K. B. R.; Subbanna G. N.; Rao T. N. G.; Rao C. N. R. *J. Mater. Res.* **1990**, *5*, 2718.
(3) Lee, C. K.; Sinclair, D. C.; West, A. R. *Solid State Ionics* **1993**, *62*, 193.
(4) Joubert, O.; Jouanneaux, A.; Ganne, M. *Mater. Res. Bull.* **1994**, *29*, 175.
(5) Vannier, R. N.; Mairesse, G.; Abraham, F.; Nowogrocki, G.; Pernot, E.; Anne, M.; Bacmann, M.; Strobel, P.; Fouletier, J. *Solid State Ionics* **1995**, *78*, 183.
(6) Abraham, F.; Boivin, J. C.; Mairesse, G.; Nowogrocki, G. *Solid State Ionics* **1990**, *40/41*, 934.
(7) Lazure, S.; Vernochet, Ch.,; Vannier, R. N.; Nowogrocki, G.; Mairesse, G. *Solid State Ionics* **1996**, *90*, 117.
(8) Galy, J.; Enjalbert, R.; Millán, P.; Castro, A. *C. R. Acad. Sci. Paris* **1993**, *317*, 43.
(9) Joubert, O.; Jouanneaux, A.; Ganne, M. *Nucl. Instrum. Methods Phys. Res.* **1995**, *B97*, 119.
(10) Satto, C.; Millet, P.; Sciau, P.; Roucau, C.; Galy, J. *Mater. Res. Bull.* **1999**, *34*, 655.
(11) Mairesse, G. In *Fast Ion Transport in Solids*; Scrosati, B., et al., Eds.; Kluwer: Dordrecht, The Netherlands, 1993; p 271.

10.1021/cm0003929 CCC: $20.00
Published on Web 12/12/2000

Table 1. Compositional Data and Lattice Parameters of the $Bi_4V_{2-x}Fe_xO_{11-\delta}$ Compounds

x	$(11-\delta)_{nominal}$[a]	$(11-\delta)_{Exp}$[b]	*a* (Å)	*b* (Å)	*c* (Å)
0	11	10.95	5.527	5.604	15.28
0.1	10.9	10.86	5.513	5.585	15.32
0.2	10.8	10.75	5.543	5.565	15.41
0.3	10.7	10.65	5.536		15.425
0.4	10.6	10.54	5.529		15.44
0.5	10.5	10.46	5.539		15.51
0.6	10.4	10.36	5.531	5.564	15.54
0.7	10.3	10.25	5.529	5.570	15.545
0.8	10.2	10.15	5.532	5.565	15.58
0.9	10.1	10.05	5.540	5.563	15.59

[a] Nominal composition of the samples assuming V^V and Fe^{III}. [b] The experimental data correspond to the set of values determined by chemical analysis. The bismuth sublimation when heating led to erroneous determination of the oxygen content by thermogravimetric analysis.

the specific role of each dopant do need the results of a crystallographic detailed study by means of techniques such as electron microscopy, EXAFS spectroscopy, and Raman spectroscopy. Detailed structural information available in the literature is rare and sparse, although there are some diffraction studies on γ-BICOVOX[12] and EXAFS measurements on different γ-BIMEVOX.[13]

Huvé et al.[14] have investigated the transformation $Bi_4V_2O_{11} \rightarrow Bi_4V_2O_{10.66}$ by means of high-temperature electron microscopy (HT-TEM), high-resolution electron microscopy (HREM), and in situ X-ray diffraction. Additional evidence corroborating the structural details of the reduced phase was obtained from vanadium-NMR experiments.[15]

In this sense, the present contribution reports detailed studies on $Bi_4V_{2-x}Fe_xO_{11-\delta}$ compounds ($0 \le x \le 0.9$, $0 \le \delta < 1$) by using electron diffraction and high-resolution electron microscopy as techniques to obtain local structural information.

Experimental Section

The samples of composition $Bi_4V_{2-x}Fe_xO_{11-\delta}$ ($0 \le x \le 0.9$, $0 \le \delta < 1$) were prepared by the solid-state reaction of Bi_2O_3 (Merck, 99.9%), V_2O_5 (Merck, 99.9%), and Fe_2O_3 (Merck, 99.9%). Previously dried stoichiometric amounts of initial reagents were ground, and the mixture was pressed into a pellet and reacted in platinum crucibles with intermediate regrinding. The sequence of the heating treatment was 600, 700, and 800 °C during 12 h on each step. The $x = 0$ sample was then additionally treated at 800 °C in flowing oxygen for 6 h and slowly cooled (10 °C/min) to room temperature in the same atmosphere. [The oxidizing treatment was performed in order to minimize the $V^V \rightarrow V^{IV}$ transformation.] The iron-doped samples were, instead, heated at 850 °C during 1 day to achieve complete reaction.

The oxygen content of the samples were determined by both thermogravimetric as well as chemical analysis by titration after dilution in 3 N HCl with Mohr's salt. Thermogravimetric analysis was developed on the basis of a Cahn D-200 electrobalance, by working in H_2/He atmosphere at 700 °C. Table 1 shows the nominal as well as the experimental anionic compositions for all the samples prepared. The total amount of bismuth, vanadium, and iron was determined by inductive coupling plasma (ICP) as well as by EDS X-ray microanalysis carried out on both a JEOL 2000 FX electron microscope supplied with a Link analyzer AN10000 and a Philips CM20 FEG SuperTwin electron microscope supplied with an EDAX analyzer DX-4, resolution ≈135 eV, and Super Ultra Thin window.

Powder X-ray diffraction (XRD) was performed on a Philips X'PERT diffractometer equipped with a bent copper monochromator and using Cu Kα radiation.

Selected area electron diffraction (SAED) was carried out on a JEOL 2000 FX electron microscope. High-resolution electron microscopy (HREM) was performed on both a JEOL 4000EX and a Philips CM20 FEG Super Twin electron microscopes. The samples for electron microscopy were ultrasonically dispersed in *n*-butanol and transferred to carbon-coated copper grids.

Results and Discussion

The structural characterization by means of powder X-ray diffraction reveals, at first sight, the $Bi_4V_{2-x}Fe_xO_{11-y}$ system to behave as a solid solution in the compositional range $0 \le x \le 0.9$. The evolution of the cell parameters shows, however, two consecutive phase transitions as a function of the doping rate *x* (see Table 1). From $x = 0$ to $x = 0.2$ the orthorhombic symmetry of the α-type $Bi_4V_2O_{11}$ structure is maintained. In the range $0.3 \le x \le 0.5$, the symmetry of the unit cell changes to tetragonal. A second orthorhombic domain appears from $x = 0.6$ to $x = 0.8$, which shows structural differences with the first that will be commented on below. For the $x = 0.9$ composition, the XRD pattern can be assigned on the basis of a $Bi_4V_2O_{10}$-type cell.[8]

As observed in Table 1, the chemical analysis of the materials shows anionic compositions corresponding to $x/(2-x) \approx$ [Fe(III)]/[V(V)] in the whole doping range. The anionic stoichiometry ranges from $\approx O_{11}$ for the undoped material to a composition close to O_{10} for $x = 0.9$. This change in the oxygen content is the same as that allowed in $Bi_4V_2O_{11-\delta}$ ($0 \le \delta \le 1$) when heating in reducing atmosphere.[8,9]

Taking into account the above information, the microstructural study of all the materials synthesized by means of electron diffraction (SAED) and electron microscopy (HREM) was performed. We tried on one hand to establish the relationship, if existing, between the microstructure of the $Bi_4V_{2-x}Fe_xO_{11-\delta}$ and $Bi_4V_2O_{11-\delta}$ systems and on the other hand to study the possible order−disorder situations associated with the presence of both Fe(III) and anionic vacancies in the perovskite-type layers of the basic structure.

When studied by electron microscopy, the series appear to behave in a much more continuous way than shown by XRD. Although the SAED patterns confirmed the unit cell dimensions previously determined, the electron micrographs show a more complex situation.

Figure 1a,b corresponds to the [001] and [100] reciprocal lattice projections of a crystal of the $x = 0.1$ composition, respectively. Figure 1c shows the [100] zone axis for an undoped crystal. Despite the information obtained by XRD, the comparison between them reveals the disappearance of the 6-fold commensurate modulation along b^* which is characteristic of the α-$Bi_4V_2O_{11}$ structure. Two diffuse diffraction maxima are observable, however, at approximatively $1/3b^*$ and $2/3b^*$.

(12) Abrahams, I.; Krok, F.; Nelstrop, J. A. G. *Solid State Ionics* **1996**, *90*, 57.
(13) Chadwick, A. V.; Colli, C.; Maltesse, C.; Morrison, G.; Abrahams, I.; Bush, A. *Solid State Ionics* **1999**, *119*, 79.
(14) Huvé, M.; Vannier, R. N.; Nowogrocki, G.; Mairesse, G.; Van Tendeloo, G. *J. Mater. Chem.* **1996**, *6*, 1339.
(15) Zhou, W.; Jefferson, D. A.; He, H.; Yuan, J.; Smith, D. J. *Philos. Mag.* **1997**, *75*, 105.

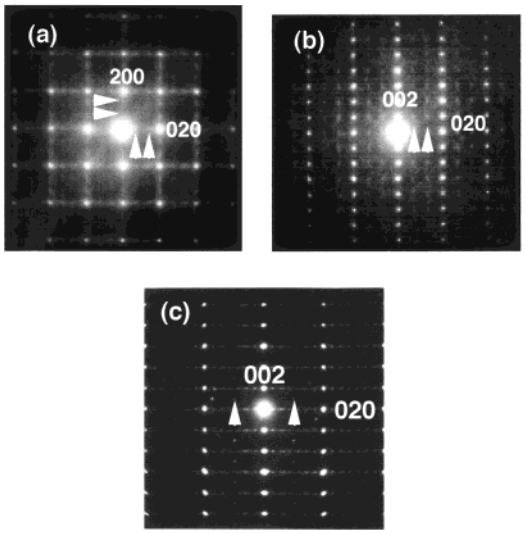

Figure 1. SAED patterns of a crystal of the $x = 0.1$ composition taken along the (a) [001] and (b) [100] zone axes. (c) SAED pattern of a crystal of the $Bi_4V_2O_{11}$ composition taken along the [100] zone axis. The central spot, marked with an arrow, indicates the beggining of the reduction process under the electron beam. (Miller indexes have been assigned corresponding to the basic unit cell of the $n = 1$ Aurivillius term.)

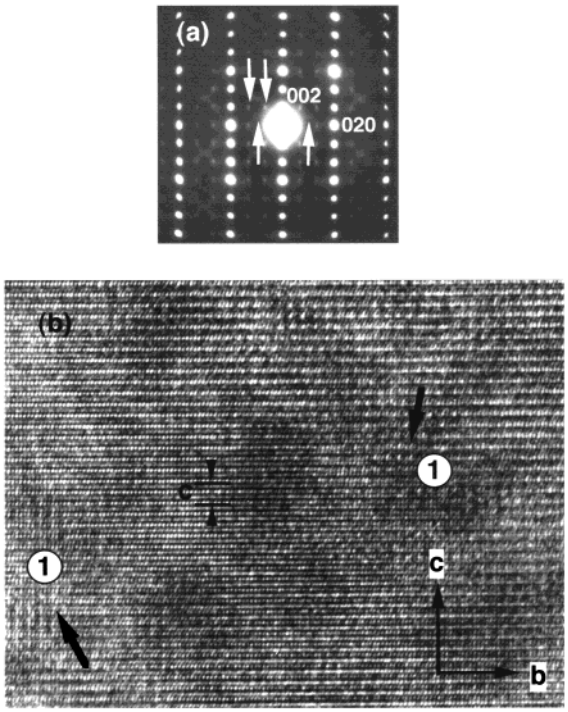

Figure 2. (a) SAED pattern of a crystal of the $x = 0.3$ composition taken along the [100] zone axis. (b) Corresponding high-resolution image. Domains ① are labeled as explained in the text.

The same features were observable for the $x = 0.2$ composition.

When the iron content was increased, slight changes in the reciprocal lattice can be appreciated. Figure 2a corresponds to the electron diffraction pattern of a crystal of $x = 0.3$ composition taken along the [100] zone axis. The diffuse maxima tripling the b^* axis can be also observed, and in addition, an extra spot appears doubling the [011]* direction. The corresponding HREM image is shown in Figure 2b. Small regions are observed

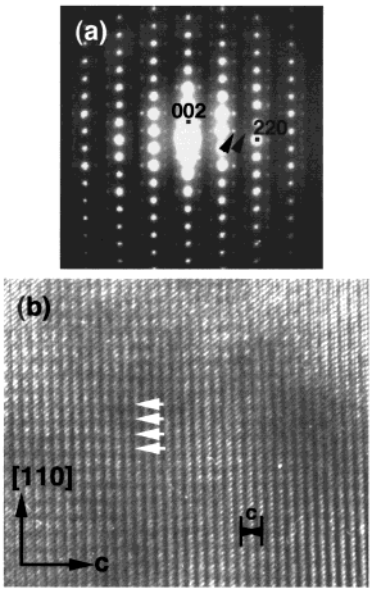

Figure 3. (a) SAED pattern of $Bi_4V_{1.7}Fe_{0.3}O_{10.25}$ in the $[1\bar{1}0]$ projection. (b) Corresponding image showing the modulation direction.

where a 3-fold superstructure along b is clearly visible (① in the image). Optical diffraction performed on these areas reveals, however, the absence of the difuse maximum doubling the [011]* direction. The remaining parts of the crystal show a contrast variation which can be assimilated to the basic structure of the $n = 1$ Aurivillius phase, but a careful examination together with the optical diffraction study corroborates the origin of the diffraction maximum doubling [011]* (we will refer in what follows to domains ②; they are not labeled in the image since they are not easy to observe as we will discuss below).

The SAED pattern taken along the $[1\bar{1}10]$ zone axis is shown in Figure 3a for a crystal of the $x = 0.3$ composition. Besides the stronger diffraction maxima corresponding to the basic supercell, some extra spots of lower intensity appear, which correspond to the first and the second diffraction order of a 3-fold commensurate modulation along [110]*. The corresponding HREM image can be observed in Figure 3b. In the thicker areas of the crystal, dark fringes equally spaced at $\approx 3d_{110}$ are clearly distinguished (marked with arrows).

The $x = 0.4$ and $x = 0.5$ compositions present equivalent microstructural features.

When almost one-third of vanadium is substituted by iron in the mother compound, i.e., $x = 0.6$, and up to $x = 0.8$, diffraction maxima previously described as diffuse become sharp and intense. Figure 4a shows the SAED pattern of a crystal of the $x = 0.7$ composition taken along the [100] zone axis; the 3-fold superstructure along [010]* is now clearly observed as well as the maximum doubling the [011]* direction. The HREM image corresponding to the same projection (Figure 4b) shows the crystal to be formed by the intergrowth of two different kind of domains each of them with a well-defined microstructure; areas labeled ① and ② correspond to regions where b is tripled and regions where [011] is doubled, respectively. A detailed analysis of the contrast in both regions reveals they are the same domains previously observed for lower iron content

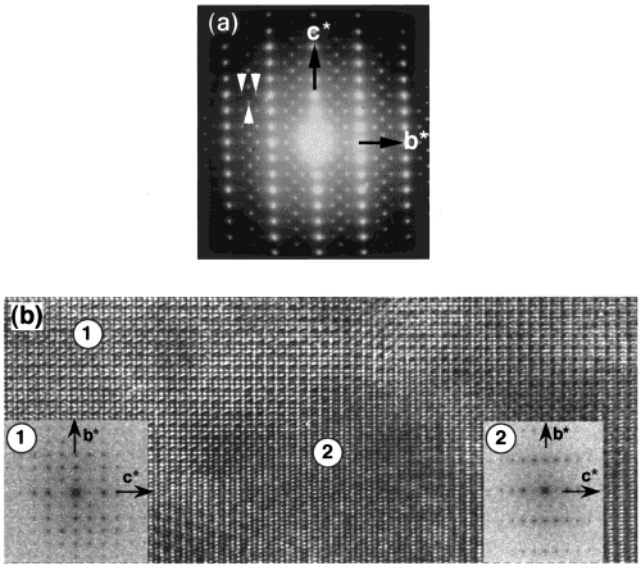

Figure 4. (a) SAED pattern of a crystal of the $x = 0.7$ composition taken along the [100] zone axis. (b) High-resolution electron micrograph in the same projection. Domains ① and ② are labeled as well as the corresponding optical diffraction patterns shown in the inset.

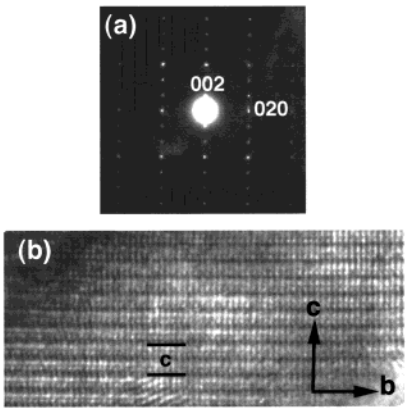

Figure 5. (a) SAED pattern of a crystal of the $x = 0.9$ composition in the [100] reciprocal projection. (b) Corresponding electron micrograph.

although their relative size has increased notoriously. The optical diffraction patterns of microstructure ① and ② have been also included.

The 3-fold modulation along [110]* can also be observed, but now only the first-order diffraction maximum is visible.

The $x = 0.9$ composition behaves in a different way. Although the XRD pattern can be indexed on the basis of a $Bi_4V_2O_{10}$-type phase, the electron microscopy study reveals a reciprocal lattice like the one shown in Figure 5a in the [100] projection. From the absence of superstructure maxima, the diffraction pattern is equivalent to the one obtained for the $n = 1$ member of the Aurivillius family Bi_2WO_6 or Bi_2MoO_6,[16] in the same projection. Figure 5b corresponds to the HREM micrograph in the above projection, and the observed contrast variation corroborates the unit cell.

Therefore, the results obtained with the microstructural characterization techniques employed showed that

(16) Knight, K. S. *Mineral. Mag.* **1992**, *56*, 339.

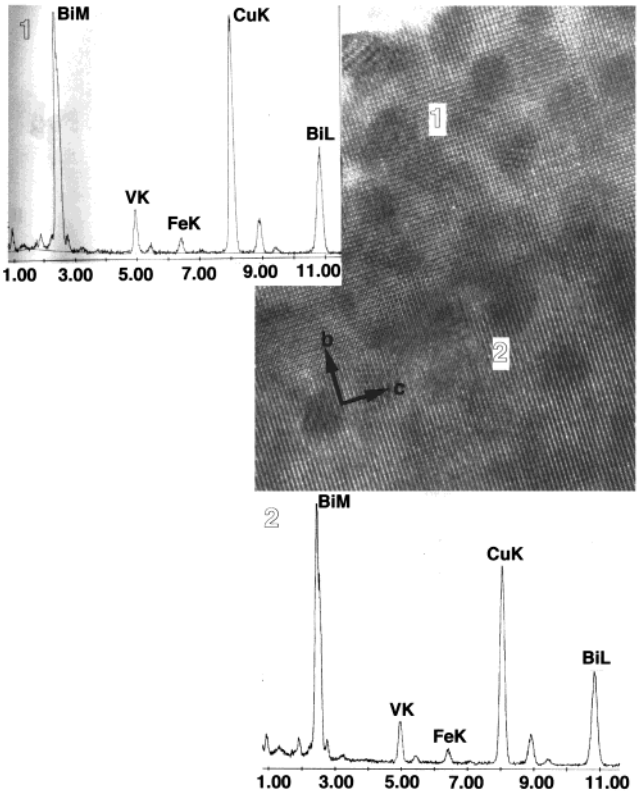

Figure 6. High-resolution low-magnification image of a crystal of the $x = 0.7$ composition, showing domains ① and ②. EDX spectra corresponding to the two microstructures have been included.

materials in the $Bi_4V_{2-x}Fe_xO_{11-\delta}$ series were formed by a unique type of crystals although heterogeneous at atomic scale, the degree of heterogeneity changing as a function of the iron content. These observations led us to relate the two different microstructures with a preferential distribution of iron, thus thinking of the doping process not as a simple isomorphous substitution process.

From the above, a careful chemical analysis of the crystals by means of EDS X-ray microanalysis was performed. Figure 6 shows a high-resolution low magnification image of a crystal corresponding to the $x = 0.7$ composition. Domains ① and ② can be observed. Besides the image, the EDX spectra of the two microstructures are also shown. Comparison between both reveals there is no difference in the relative intensity of the characteristic emission lines of each element. Moreover, the semiquantitative analysis of the Fe:V ratio shows ≈32% of iron in the two type of regions, a ratio that is in good agreement with the nominal composition, $Bi_4V_{1.3}Fe_{0.7}O_y$. At this point, it is worth mentioning that the microstructural features of these materials, as well as the relative size of the domains, made the analysis easier in the samples with higher iron content. However, the equivalence of the contrast observed for both microstructures in the whole series allowed us to extend the above results to all the compositions studied.

We conclude, then, that iron and vanadium are randomly distributed in the B sublattice and, therefore, microstructural differences should not be related to the preferential location of any of the two metallic elements.

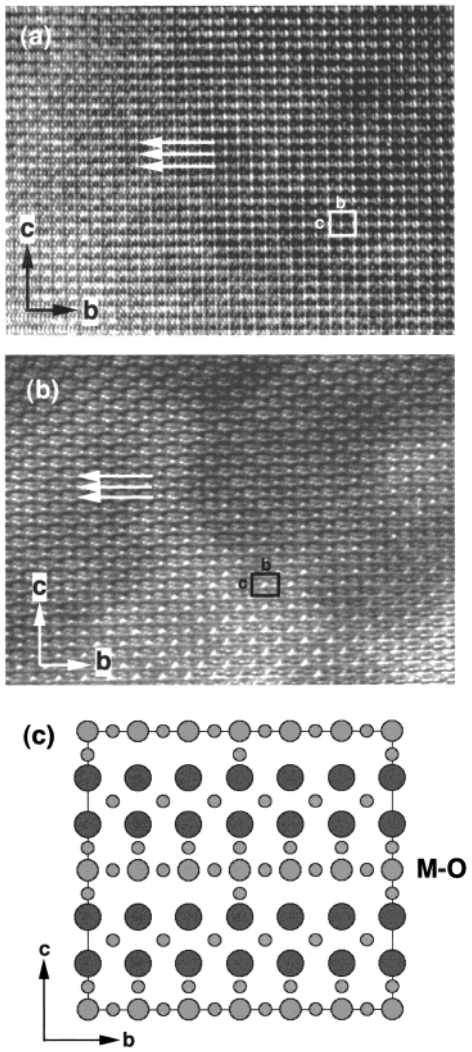

Figure 7. HREM images of (a) one domain ① and (b) $Bi_4V_2O_{10.66}$, taken along the [100] zone axis. (c) Simplified structure model proposed for domain ①.

Taking into account the above results and provided that the anionic stoichiometry of the samples diminishes as the iron content increases (see Table 1), we tried to interpret the two microstructures observed in terms of short-range−long-range ordering of the anionic vacancies in the perovskite layers of the basic structure.

In the composition range $0.1 \leq x \leq 0.3$, the anionic stoichiometry varies between $O_{10.85}$ and $O_{10.65}$. Provided that the limit is very close to $O_{10.66}$, and taking into account the fact that in both $Bi_4V_{2-x}Fe_xO_y$ ($0.1 \leq x \leq 0.3$) and $Bi_4V_2O_{10.66}$ a 3-fold superstructure along *b* appears, we first tried to compare the contrast in regions type ① with those of the undoped compound $Bi_4V_2O_{10.66}$. Figure 7a,b shows in a comparative way the HREM images of domain ① and $Bi_4V_2O_{10.66}$ in the [100] projection, respectively. As evidenced, the most characteristic feature of the $O_{10.66}$ compound, i.e., the sinusoidal contrast given by the V−O layers (see Introduction), is not observed in domains ① of the doped materials. Taking into account that both V(V) and Fe(III) can adopt 4-, 5-, and 6-fold coordination, there exist two ordered sequences of V/Fe−O polyhedra, which generating a 3-fold superstructure along *b* are compatible with the average oxygen content of the samples: (i) a sequence constituted by two tetrahedra and one octahedron, which corresponds to O_{10} anionic composition; (ii) a sequence formed by two square pyramids and one octahedron, corresponding to the $O_{10.66}$ stoichiometry.

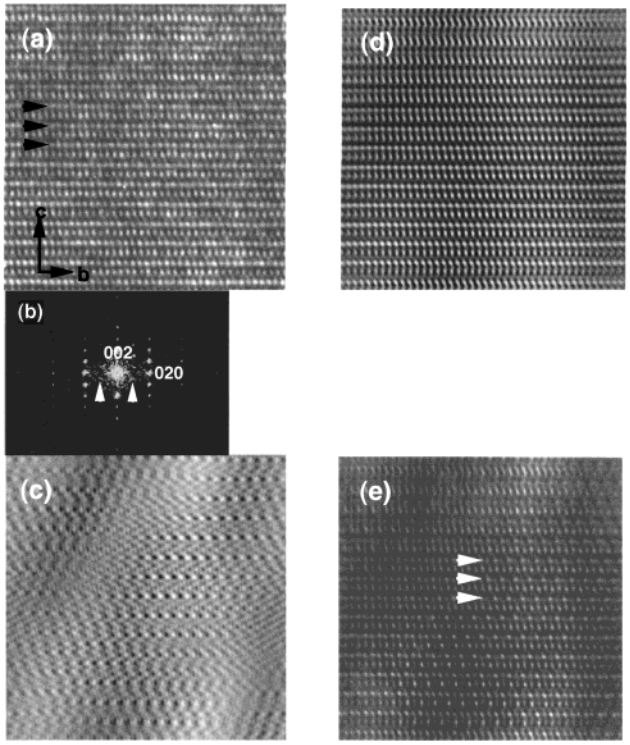

Figure 8. (a) Magnified image of one domain ② in the [100] projection. (b) Fourier transform of the area shown in (a). (c) Image reconstruction from the (0*kl*), *l* and $k = 2n$ diffracted beams. (d) Image reconstruction from the (0*kl*), *l* and $k = 2n + 1$ diffracted beams. (e) Overlapping of images shown in (c) and (d).

At this point, we should consider the analysis of the image contrast in domains ②. The optical diffraction pattern on these domains (see inset in Figure 4b) showed a diffuse maximum doubling the [011]* direction. However, the examination of the contrast variation along [011] does not show at first glance the corresponding 2-fold superstructure. Image processing by Fourier filtering followed by image reconstruction provides a way of reducing random noise in an HREM image and increase image contrast averaging over a large number of unit cells with identical orientation. Figure 8a corresponds to an enlarged image of the domain ② taken from a crystal of $x = 0.7$ composition in the [100] projection. The Fourier transform on this area is shown in Figure 8b, and the (011) diffraction maximum can be observd (marked with an arrow). When the (0*kl*) diffracted beams with *k* and $l = 2n$ are selected, the inverse Fourier transform gives rise to the image shown in Figure 8c. If only the (0*kl*) maxima are selected where *k* and $l = 2n + 1$, image reconstruction corresponds to Figure 8d. Overlapping of images c and d results in Figure 8e. The 1:1 alternance of bright and dark contrast is now clearly observed in the V/Fe−O layers (marked with arrows), and this alternance is inverted from one layer to the next. This effect is the reason for the [011] direction to be doubled.

To interpret the above features we considered again an ordered distribution of anionic vacancies in the

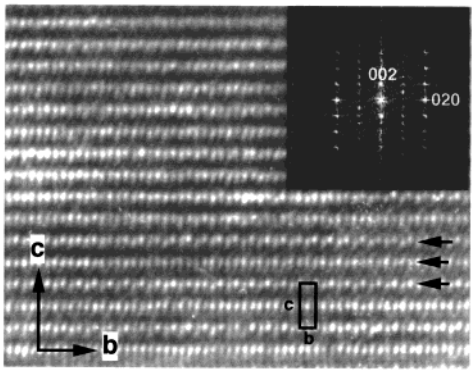

Figure 9. Enlarged area of a crystal of the $Bi_4V_2O_{10}$ composition in the [100] projection. The corresponding optical diffraction pattern has been included as an inset.

perovskite-type layers of the structure, which can give rise to the superstructure observed.

Figure 9 shows an enlarged area of a crystal of the $Bi_4V_2O_{10}$ composition[17] together with the corresponding optical diffraction pattern, in the [100] projection. Comparison is done with Figure 8e,b, respectively. The characteristic alternance of dark and bright contrast is clearly observed in the image of the $Bi_4V_2O_{10}$ compound, where the V−O layers are exclusively constituted by VO_5 pyramids. The diffraction patterns can also be compared, although the (*hkl*) maxima with $(k + l) = 2n$ do not appear for the doped sample, a fact that can be associated with the cell centering.

From the previous discussion one can interpret the microstructure of domains ② as formed by a unit cell of parameters close to 5.4 × 5.5 × 15.5 Å, similar to that of the $Bi_4V_2O_{10}$ compound in the sense that the M−O layers are formed by corner sharing MO_5 square pyramids randomly occupied by Fe and V.

If O_{10} is the average oxygen composition of domains ② and taking into account both the decreasing oxygen content of the materials as the iron content increases and the growing size of the two types of areas, it seems reasonable to think about a higher anionic composition to interpret the microstructure of domains ①. From the two sequences previously proposed, the one leading to $O_{10.66}$ anionic composition is compatible with the above discussion.

The study of the reciprocal space of domains ① and the observed diffraction conditions allowed us to propose the noncentrosymmetric space group *Fmm*2 (No. 42) as the most probable. Atomic positions associated to this symmetry group were used to deduce the ideal atomic coordinates of the structure model proposed (Figure 7c). They were further used as input data in the simulation of the reciprocal space.[18] Figure 10a,b shows the calculated electron diffraction patterns in the [100] and [01$\bar{1}$] projections, respectively. The 3-fold superstructure along *b* is clearly observed as well as the analogy with the corresponding inset in Figure 4b. However, diffraction maxima coming from the modulation along [110]* are not observable. This fact can be explained if one takes into account that calculation has been done considering a perfectly ordered distribution of the anionic vacancies

(17) García-González, E.; Arribas, M.; González-Calbet, J. M. To be published.
(18) Mac Tempas software package.

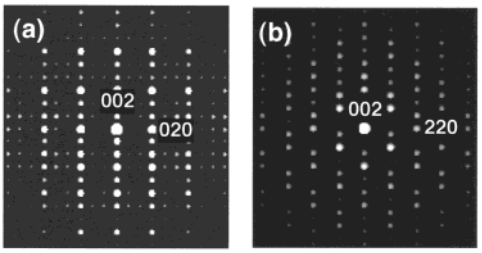

Figure 10. Calculated electron diffraction patterns for the structure model proposed for domain ① in the (a) [100] and (b) [01$\bar{1}$] projections.

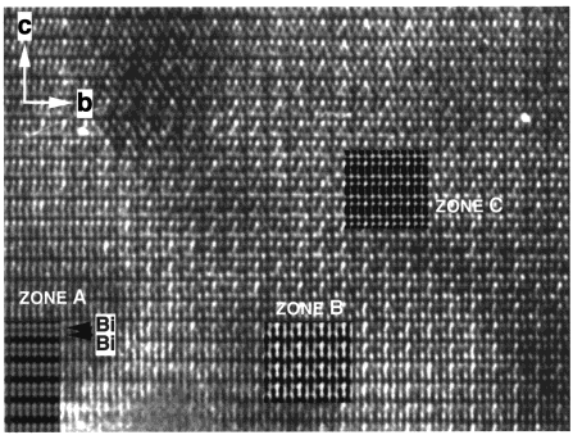

Figure 11. Enlarged image of one domain ① taken from a crystal of the $x = 0.7$ composition. Calculated images for the proposed model have been included. Image conditions: A, $t =$ 3.0 nm, $\Delta f = -45$ nm; B, $t = 60$ nm, $\Delta f = -60$ nm; C, $t = 8.5$ nm, $\Delta f = -70$ nm.

inside the M−O layers along the [010] direction. But due to the polyhedra distribution itself inside the perovskite-type layers, the superstructure cannot be observed along the [110] direction because of the contrast overlaping of different coordination environments. In the observed crystals, however, coexistence of domains ① and ②, as well as their relative small size, is limiting also the contrast overlaping in the [110] direction, and therefore, a 3-fold modulation is observed instead of an ordered superstructure. This observation becomes clearer as the size of the domains becomes smaller, i.e., for lower iron contents.

Figure 11 shows an enlarged image of one domain ① taken from a crystal of $x = 0.7$ composition. Image calculation for the proposed model has been included, images labeled A, B, or C corresponding to different thickness and defocus conditions (see figure caption). In the thinnest part of the crystal (zone A) image contrast is mainly a function of the metallic atoms contribution; it has been easily matched by using a vanadium containing Bi_2WO_6-like structure[16] despite the anionic vacancies. Zones B and C, however, show the 3-fold superstructure. Using the image contrast and the known positions of the bismuth atoms in zone A as reference, and assuming structural continuity across the crystal, Bi_2O_2 layers in regions B and C could be also identified. Although atomic coordinates cannot be directly extracted from the experimental image, both the structure model proposed and the experimental contrast have been used to calculate the images shown in B and C. The experimental image presents a good fit with the calculated images.

From these results, domains ① in the crystal can be described as constituted by an ordered distribution of two square pyramids and one octahedron in the perovskite-type layers, which gives rise to the $O_{10.66}$ anionic composition.

It is worth mentioning that the structural refinement carried out by Joubert et al.[19] from powder X-ray diffraction data on $Bi_4V_{1.5}Fe_{0.5}O_{10.5}$ locates the anionic vacancies on the apical site of the perovskite-like layers and a 3-fold commensurate modulation along the *b* axis is observed. Both facts would be in agreement with our structure model to explain the microstructure of domains ①.

The interpretation given to the microstructural features of domains ① and ② can justify the average oxygen content determined by chemical analysis for the whole composition range. The previously identified phase transition $\alpha \leftrightarrow \beta \leftrightarrow \gamma$ in the interval $0.1 \leq x \leq 0.5$ [19] can be seen then as the symmetry of the average unit cell which varies when growing the relative size of the domains. For the $x = 0.9$ composition microstructure changes dramatically. The previously ordered anionic vacancies are randomly distributed now which corresponds to a Bi_2WO_6-type unit cell; the low oxygen content is probably close to the stability limit of the basic structure.

Acknowledgment. Authors are grateful to the Cantro de Microscopia Electronica (U.C.M.) for facilities. Financial support was provided by the CICYT (Spain) through Research Project MAT98-0648.

CM0003929

(19) Joubert, O.; Ganne, M.; Vannier, R. N.; Mairesse, G. *Solid State Ionics* **1996**, *83*, 199.